ACS APPLIED NANO MATERIALS

www.acsanm.org Article

Stable Chitosan and Prussian Blue-Coated Laser-Induced Graphene Skin Sensor for the Electrochemical Detection of Hydrogen Peroxide in Sweat

Robert Barber, James Davis, and Pagona Papakonstantinou*

Cite This: https://doi.org/10.1021/acsanm.3c01199 Read Online

ACCESS | Metrics & More | Article Recommendations | Supporting Information

ABSTRACT: Developing a noninvasive skin peroxide monitoring technology is highly desirable for managing a number of metabolic disorders associated with diabetes, pulmonary diseases, or other health conditions. To date, the majority of studies on peroxide detection have been conducted on simulated sweat and high pH conditions, which are beyond the physiological range, in order to provide an enhanced response. Here, a skin-worn amperometric sensor, based on laser-induced graphene (LIG), surface-engineered with a Prussian blue (PB)−chitosan (CS) network was fabricated by one-step electrodeposition for the stable and sensitive detection of H_2O_2 in human eccrine perspiration. The hybrid (PB−CS) network and laser-written electrode configuration were optimized through systematic investigation of electrodeposition parameters and concurrent feedback from electrochemical and morphological characterization at each fabrication step. Different from the multitude of carbon-based electrodes functionalized with metallic nanoparticles reported in the literature, the sensor was operated at a low potential of −0.036 V vs Ag/AgCl in unmodified human eccrine perspiration. The low working potential ensured that the sensor is highly specific, immune to the current from oxygen reduction or common interfering species, whereas the inclusion of CS in the hybrid coating afforded a highly stable performance over a period of 14 days. The sensor was able to monitor H_2O_2 over the linear range of 10−1000 μM with a low detection limit of 6.31 μM and achieved a recovery of 98.73% (% RSD 0.86) in human eccrine perspiration. This facile biosensor based on directly laser-written electrodes coupled with the one-step PB−CS fabrication strategy has the potential to form the basis for the development of oxidase enzyme-based sensors in sweat.

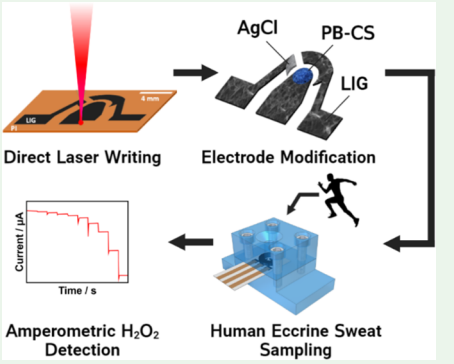

KEYWORDS: *laser-induced graphene (LIG), hydrogen peroxide, sweat, biosensor, Prussian blue, chitosan, electrochemical H_2O_2, amperometric detection, skin sensor*

1. INTRODUCTION

The current revolution of healthcare toward mobile health (m-health) has led to the development of cutting-edge wearable sensors that can provide the patient with insights into their health instantaneously, in their own home or care facility.[1−4] The available biofluids for sensing can be categorized as invasive, minimally invasive, and noninvasive corresponding to blood, interstitial fluid (ISF), and sweat, tear, or saliva, respectively. ISF wearable sensors have been successfully developed and commercialized, with sweat appearing to be the next frontier.[5] Sweat has garnered significant research interest due to the lack of sampling issues associated with tears and the large variability in saliva. In addition, sweat as a medium promises the ability to continuously monitor biomolecules without the risk of bloodborne pathogen infection or the pain associated with capillary and venous blood samples.[5] Sweat has been used to screen for cystic fibrosis through detection of abnormally high levels of chloride, but as the physiology of sweat has become better understood, further biomarkers beyond chloride have gained research interest. These include metabolites (glucose, ethanol, uric acid, lactate, peroxide), ions (sodium, potassium, magnesium, calcium),[6] and foreign substances such as therapeutic or illicit drugs. In particular, current studies are focused on the development of on-skin flexible sensors worn by the user that can provide real-time assessment of their metabolism and/or monitor the levels of their therapeutic medication continuously.[7−9]

Hydrogen peroxide (H_2O_2) is produced in various cellular processes, but when it is generated at high concentrations, it causes oxidative damage with consequent disease onset; hence, measurements of H_2O_2 in body fluids are relevant for health diagnostics. It is considered an important biomarker because of its involvement in various biological processes such as physiological signaling and immune response. Any imbalance

Received: March 17, 2023
Accepted: May 25, 2023

in its production and consumption can induce deleterious effects on important cellular structures and has been implicated in various disease conditions such as cardiovascular disease, cancer, aging, and neurological disorders such as Parkinson's and Alzheimer's diseases. H_2O_2 is also a byproduct of various enzyme-catalyzed reactions, generated in proportional amounts to the target metabolite concentration. As a result, electroanalytical quantification of H_2O_2 has been well-documented on rigid[10−16] and flexible[17−22] substrates and is the target of numerous diagnostic kits involving various oxidases such as glucose oxidase, alcohol oxidase, lactate oxidase, and cholesterol oxidase for the indirect detection of various metabolites.[23,24] However, all of these enzymes require strict physiological conditions for performing catalytic functions. Their limited stability in harsh environmental conditions (pH, temperature, light), the high cost of synthesis, isolation, and purification are some of the significant drawbacks to their use in enzyme-based electrochemical sensors for H_2O_2 detection.

Nevertheless, direct amperometric detection of H_2O_2 is achievable at relatively high ≈0.6 V (vs Ag/AgCl) using conventional noble metal (e.g., Au, and Pt) electrodes. However, at this high potential, selectivity for H_2O_2 is hampered by the oxidation of other electroactive species (e.g., ascorbic acid (AA) and uric acid (UA)). At large negative overpotentials, the reduction of dissolved oxygen is known to interfere with the measurement of H_2O_2 concentration. Recently, metallic (Pt, Cu, Ag, Au) nanoparticle coatings have been utilized on graphene-based electrodes to detect H_2O_2[19−21,25] (Table S2). While these approaches demonstrate a significant improvement in sensitivity, when compared to their planar metallic electrode counterparts, the drawbacks associated with large detection potentials persist.

As an alternative to a redox mediator, Prussian blue (PB, $Fe_4[Fe(CN)_6]_3$) in its reduced form, Prussian white (PW, $Fe_4K_4[Fe(CN)_6]_3$), is commonly used to catalyze the reduction of H_2O_2 at low overpotentials.[26−28] The mechanism for the reduction of PB to PW (eq 1a) and the subsequent reduction of H_2O_2 (eq 1b)[29] that occurs at a low potential hence mitigate the large interfering current from the reduction of dissolved oxygen, or oxidation of other interferences, found in biological solutions.

$$Fe_4[Fe(CN)_6]_{3(PB)} + 4e^- + 4K^+ \rightleftharpoons Fe_4K_4[Fe(CN)_6]_{3(PW)} \quad (1a)$$

$$Fe_4K_4[Fe(CN)_6]_{3(PW)} + 2H_2O_2 \rightleftharpoons Fe_4[Fe(CN)_6]_{3(PB)} + 4OH^- + 4K^+ \quad (1b)$$

Equation 1: Generation of Prussian white (a) allowing the catalytic reduction of hydrogen peroxide (b).

PB has an open-framework hexacyanometalate crystal structure with the general chemical formula $A_xFe(II)[Fe(III)\text{-}(CN)_6]_{1-y}\cdot zH_2O$, where A is an alkali ion, like potassium (K), which can reversibly be inserted into the interstitial sites of the framework; the iron atoms are in two different oxidation states (Fe(II), Fe(III)) interconnected by C−N pairs. The large interstitial channels aid in fast intercalation kinetics for K ions (K^+) and facilitate redox reactions for use as electron-transfer mediators. The efficient electron transfer, together with the low toxicity and easy synthesis, is an important attribute for establishing PB as an electrode modifier in biosensing fields.[30,31]

As stated earlier, PB is highly specific to the reduction of H_2O_2. At 0 V (vs Ag/AgCl), the response toward H_2O_2 has been shown to be 400−600 times the magnitude of its response to the reduction of oxygen in solution.[32] Moreover, peptides found in sweat often contain chains of amino acids that are known to permanently inactivate traditional platinum electrodes, a problem not encountered with PB.[24,33] However, a major limitation of PB-based biosensors is their short-term electrochemical stability in neutral or alkaline solutions, thus reducing their suitability for epidermal applications as the pH of sweat can vary from 4.5 to 7 and that of interstitial fluid ranges from 7.2 to 7.4.[34]

To address the solubility problem of PB for its application in long-term, in situ on-skin sensing, polymer-based membranes such as Nafion are often used to stop the outward PB diffusion. However, the negative charge of the sulfonated-based (Nafion) membrane prevents its uniform direct assembly over the negatively charged PB layer through electrostatic repulsion. An alternative strategy, involving the use of biopolymer coating, such as chitosan, on top of PB to act as a sealant layer, has occasionally been employed. Chitosan, formed from the chemical deacetylation of chitin, mostly extracted from crustacean shells, is a sustainable biopolymer with high stability and good biocompatibility.[35,36] The film-forming ability of chitosan has driven its implementation in encapsulating enzymes in biosensors.[37] The same amino groups in chitosan that protect enzymes from harsh environments are able to stabilize PB on an electrode surface in neutral environments[26,37] since the negatively charged ferricyanide PB precursor exhibits electrostatic attraction to the positively charged chitosan[26,38]

The majority of research efforts for H_2O_2 detection have been conducted on either glassy carbon or other nonintegrated sensors (i.e., traditional three-electrode system with standalone reference and counter electrodes) or conventional screen-printed electrodes (SPEs) in acidic or basic solutions. These approaches have limited applications in epidermal sensors due to requirement of a flexible integrated sensing platform with high sensitivity in neutral pH solutions such as sweat. Moreover, H_2O_2 and other important biomarkers are typically found in reduced concentrations in eccrine perspiration compared to blood plasma, hence requiring even higher sensitivity.[5] Recently, three-dimensional (3D) porous graphene patterns have been synthesized in a direct-write manner, simply by irradiating various carbon sources including food, polymers, and wood with an infrared CO_2 laser.[39−41] This material, referred to as laser-induced graphene (LIG), combines the excellent electrochemical properties of graphene-based materials with the rapid manufacturing of laser printing on flexible insulators.[42−44] LIG was pioneered by Tour's group in 2014, when they demonstrated patterned conductive tracks by irradiating a polyimide film with a commercial laser.[42] Polyimide (PI) contains numerous aromatic groups that absorb light in the infrared to ultraviolet region, enabling localized high temperatures and breaking the C−O, C═O, and N−C bonds, with a subsequent release of gases, and finally causing a transition from sp^3 to sp^2 hybridized states. Therefore, irradiation of PI in air, with a range of laser sources, leads to photothermal conversion and formation of 3D foam like graphitized structure.[43,44] When compared to edge plane pyrolytic graphite (EPPG), known as the "gold standard" of carbon materials for electrochemical applications, LIG has demonstrated a faster heterogeneous electron transfer (HET)

https://doi.org/10.1021/acsanm.3c01199
ACS Appl. Nano Mater. XXXX, XXX, XXX−XXX

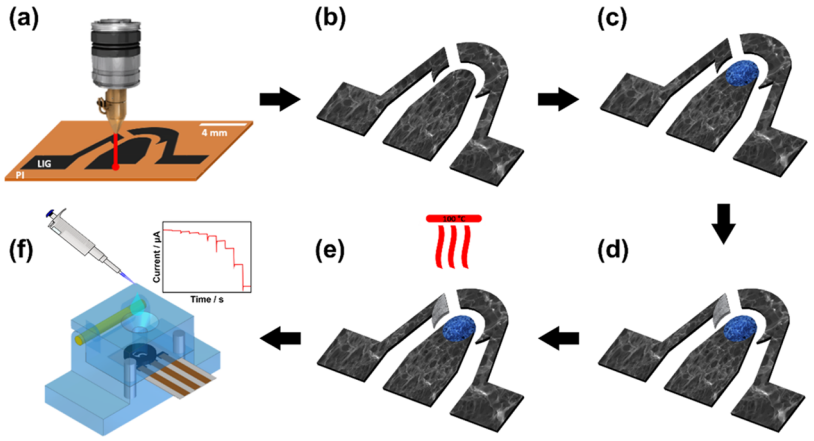

Figure 1. Fabrication steps of an integrated LIG/PB−CS sensor for H_2O_2 detection. The integrated electrode assembly was directly written onto a polyimide sheet, using a CO_2 laser (a), yielding conductive, highly porous graphitized patterns (b). The PB−CS composite coating (represented by a blue circle) was electrodeposited onto the working electrode (c), followed by drop-casting conductive silver paint onto the reference electrode (d). Heat treatment at 100 °C was used to stabilize the PB−CS coating (e). The fabricated integrated sensor was employed to analyze H_2O_2 concentration in sweat using a purposely designed electrochemical cell (f).

rate of 13 ± 1 × 10^{-3} cm s^{-1} (vs 8.8 × 10^{-3} cm s^{-1} for EPPG).[45] In addition, the highly porous structure of LIG offers an abundance of defect sites, suitable for functionalization.

Herein, we report on a flexible electrochemical platform for the sensitive electrochemical detection of H_2O_2, based on laser-induced graphene, coated with a Prussian blue/biocompatible polymer chitosan (CS) composite layer, fabricated by a simple one-step electrodeposition approach. PB and CS have been previously used in connection with enzymatic biosensors[22] in artificial sweat. Yet, to the best of our knowledge, there is no published work reporting on the one-step electrodeposition of PB−CS on LIG for epidermal sensing of peroxide in human sweat. Currently, there is no report discussing the sensitivity, specificity, and long-term stability of LIG/PB−CS flexible sensors for peroxide detection in human sweat, which are important prerequisites for epidermal biosensors. This integrated and flexible amperometric sensor is capable of performing continuous H_2O_2 detection in a complex biofluid like sweat with a detection limit of ∼6 μM at a near-zero volt detection potential. Moreover, utilizing the LIG/PB−CS as a base platform offers the opportunity for developing a flexible wearable miniaturized biosensor suitable for the detection of numerous metabolites or pathogens for on-body measurements upon further functionalization with oxidase enzymes or recognition elements.

2. EXPERIMENTAL DETAILS

2.1. Materials. A polyimide film (75 μm thick, from RS Components (U.K.)) was used to prepare the LIG. Conductive silver paint was purchased from Ted Pella (USA). Iron(III) chloride, potassium ferricyanide(III), chitosan (medium molecular weight), and hydrogen peroxide were purchased from Sigma-Aldrich and used without further purification. Britton−Robinson (BR) buffers, used due to their high buffering capacity during electrochemical characterization activities, were composed of boric acid (H_3BO_3; 99.5%; Sigma), glacial acetic acid (CH_3COOH; 99.7%; Sigma), and phosphoric acid (H_3PO_4; 85%; Sigma), all in an equimolar concentration (0.04 M) and adjusted to the required pH with concentrated sodium hydroxide (NaOH; 99.8%; Sigma).

Artificial eccrine perspiration (AEP) (Biochemazone, Canada) was used for simulated sweat characterization. Human sweat was collected from consenting male and female participants aged 18−60 years. Tegaderm + PAD nonadherent dressings were applied to the lower back of the participants during exercise; the sweat was then extracted by centrifugation and stored at −18 °C. Ethical approval for the collection of sweat for use in the characterization of electrochemical sensors was given by the Ulster University Faculty of Computing, Engineering and the Built Environment Ethics Filter Committee (CEBE_RE-21-013-B).

2.2. Electrode Design and Fabrication of Flexible LIG Electrodes. Single and integrated LIG electrodes were designed using AutoCAD software and fabricated from polyimide film sheets using a ULS CO_2 25 W VLS230 laser system (Arizona) under atmospheric conditions. Polyimide was selected due to its ubiquitous use in the electronics industry. The material is inexpensive and readily available, with strong batch-to-batch consistency. Unless otherwise stated, the optimized laser irradiation parameters were identified at a power of 7.5 W, a raster speed of 50.8 cm/s, and a repetition rate of 1000 pulses per inch, with a spot size (diameter) of 76 μm per pulse. Electrodes were connected to the potentiostat by copper tape with a silver paste coating at the copper/LIG interface to ensure good ohmic contact. The working area of an electrode was defined by sealing the LIG substrate in a laminated pouch with a 3 mm-diameter circular aperture as previously described.[46]

The integrated electrode flexible sensor assembly was fabricated in a similar manner, with all three electrodes (working, counter, and reference) laser-written onto a single piece of polyimide. The laser-written reference electrode was drop-cast with silver paint, followed by submersion in a KCl/HCl solution to induce chlorination of the Ag layer. This pseudo-reference electrode exhibited an ∼80 mV negative shift compared to a standard glass 3 M KCl Ag/AgCl BASi as demonstrated in Figure S1. The laser-written counter electrode was used without further modification. A laminate with a 7 mm circular aperture isolated the three laser-written electrodes from their electrical Ag/Cu contacts.

2.3. Functionalization of LIG Electrodes with Prussian Blue−Chitosan Coating. The LIG working electrode was functionalized via a one-step electrochemical process, simultaneously depositing a hybrid Prussian blue−chitosan (PB−CS) coating. Toward this end, working electrodes were first anodized at 2 V (vs Ag/AgCl) using a Pt wire as the counter electrode in 0.1 M NaOH for 60 s. This anodization process improved the performance of pristine LIG, as discussed later. Following rinsing in distilled water (dH_2O), the electrodes were placed in a mixture of Prussian blue (PB) and chitosan (CS) solution (the PB solution consisted of 2.5 mM $FeCl_3$, 2.5 mM $K_3Fe[CN_6]$, 0.1 M KCl, and 0.01 M HCl; the CS solution consisted of 0.01% chitosan in 1% acetic acid), and a potential of +0.4 V (vs Ag/AgCl) was applied for 300 s, yielding the electrodeposition of a homogeneous PB−CS matrix. Following PB−CS deposition, the

https://doi.org/10.1021/acsanm.3c01199
ACS Appl. Nano Mater. XXXX, XXX, XXX−XXX

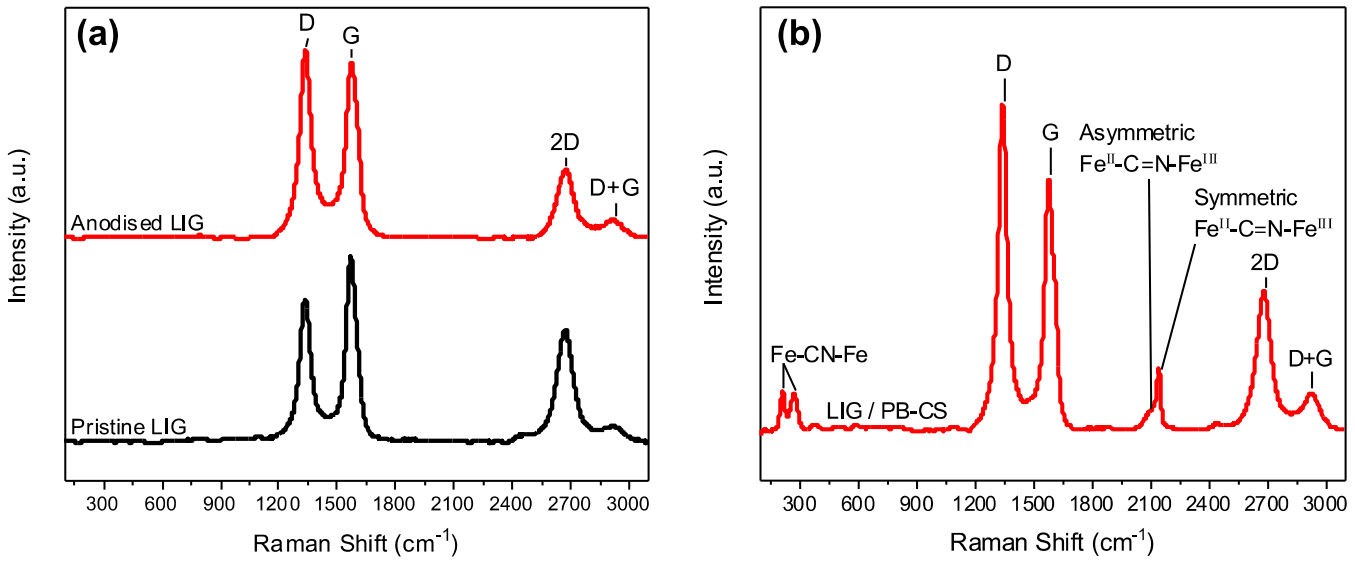

Figure 2. Raman characterization. Raman spectra of LIG before and after anodization in alkaline media (0.1 M NaOH) for 60 s, demonstrating an increase in the I_D/I_G ratio (a). Raman spectra of the LIG electrode after electrodeposition of the hybrid PB−CS coating, demonstrating the development of PB peaks (b).

electrodes were rinsed with distilled water (dH_2O) to remove weakly adsorbed PB and were subjected to repeated cyclic voltammograms in a supporting electrolyte solution (0.1 M KCl + 0.01 M HCl) from −0.25 to +0.65 V (vs Ag/AgCl) at 0.05 V/s until stable peaks were achieved. After further cleaning with dH_2O, the electrodes were heated at 100 °C for 60 min to remove residual water and stored at 4 °C. The working electrodes of the integrated sensors were fabricated using the same pretreatment and deposition conditions, as illustrated in Figure 1. In the integrated electrode, the PB−CS coating was added to the working electrode first. Only the working electrode of the integrated electrode was connected to the potentiostat (with Ag/AgCl and Pt wire completing the setup) during the deposition. The pseudo-reference electrode was formed after the completion of the PB−CS deposition and post-treatment steps.

2.4. Electrochemical Experiments. All cyclic voltammetry (CV) and chronoamperometry (CA) measurements were carried out at 22 ± 2 °C. Electrochemical measurements were conducted on an Autolab PGSTAT20 potentiostat using a three-electrode configuration with fabricated LIG as the working electrode. Initially, a platinum wire counter electrode and a glass-body Ag/AgCl reference electrode (3 M KCl, BASi) completed the three-electrode configuration. After optimization of the LIG/PB−CS fully integrated sensor, which included a AgCl pseudo-reference electrode, all CV and CA measurements for the detection of H_2O_2 were completed having the potentiostat terminals connected to the respective working, counter, and reference electrodes of the integrated sensor. A customized electrochemical cell (illustrated in Figure S2), machined from acrylic, was used for integrated electrode CA measurements; this facilitated a ∼500 μL detection volume, simulating the small volumes of sweat available for wearable sensors. A 7 mm-diameter aperture of the integrated electrode resulted in a minimum cell volume of ∼10 μL as only a drop of solution was required to cover the integrated counter, working, and reference electrodes. The electrode was sandwiched between the two pieces of the acrylic cell, where an O-ring on the top piece compressed the electrode surface, when the cell was closed, forming a liquid-tight seal. All electrochemical measurements were completed without stirring, with the exception of continuous addition chronoamperometry measurements, where magnetic stirring at 200 RPM was employed throughout. The Britton−Robinson buffer was selected over phosphate-buffered saline (PBS) for some experiments as the former is a multibuffer system that enables the pH of the solution to be easily modified by the addition of concentrated sodium hydroxide. The resultant solution has a wider buffering range than PBS and is better able to maintain the pH despite small changes in the environment during electrochemical experiments.

2.5. Surface Analysis. Single modified working electrodes were characterized by Raman microscopy and X-ray photoelectron spectroscopy (XPS) to determine the chemical composition and electronic structure of the hybrid PB−CS coating. These findings were used toward the design of the integrated sensor. Raman microscopy was employed to probe the electronic structure of working electrodes at each step of the fabrication process and was performed with a Renishaw Raman microscope equipped with a 45 W, 532 nm laser operated at 10% power. Scanning electron microscopy (SEM) performed with Hitachi SU5000 FE-SEM was used to study the surface morphology of LIG. In addition, SEM was used to optimize and critically select the electrode geometries and PB−CS deposition parameters used in the fabrication of the integrated sensor. Energy-dispersive X-ray spectroscopy (EDS) analysis and maps were obtained using an Oxford Instruments system integrated to a Hitachi SU5000 FE-SEM. X-ray photoelectron spectroscopy (XPS) was employed to investigate the chemical bonding configurations of the electrode surface after each preparation step. The spectra were acquired with a Thermo Scientific ESCALAB Xi$^+$ spectrometer. The X-ray source was a monochromatic Al Kα ($h\nu$ = 1486.6 eV, >900 um spot size) operating at 225 W (15 kV and 15 mA). Charging effects were adjusted by setting the lowest binding energy for the entire C 1s spectral envelope to 284.8 eV, commonly accepted as adventitious carbon surface contamination. Data analysis and fitting of the high-resolution spectra were performed with CasaXPS software, with a Shirley background subtracted from each peak. For percentage atomic concentration calculations, the peak areas of the most intense spectral lines for each elemental species were used.

2.6. Summary of Fabrication Steps for the Integrated LIG/PB−CS Sensor. Figure 1 depicts the fabrication steps of an integrated LIG/PB−CS-based electrochemical sensor. The three-electrode design was patterned directly onto a 75 μm thick polyimide film by a CO_2 laser (Figure 1A,B). The PB−CS coating was electrodeposited onto the working electrode (Figure 1C), followed by the drop-casting of silver paint to create the pseudo-reference electrode (Figure 1D). The entire integrated sensor assembly was then heat-treated (Figure 1E) before use in H_2O_2 sensing in a specially designed small-volume electrochemical cell (Figure 1E).

https://doi.org/10.1021/acsanm.3c01199
ACS Appl. Nano Mater. XXXX, XXX, XXX−XXX

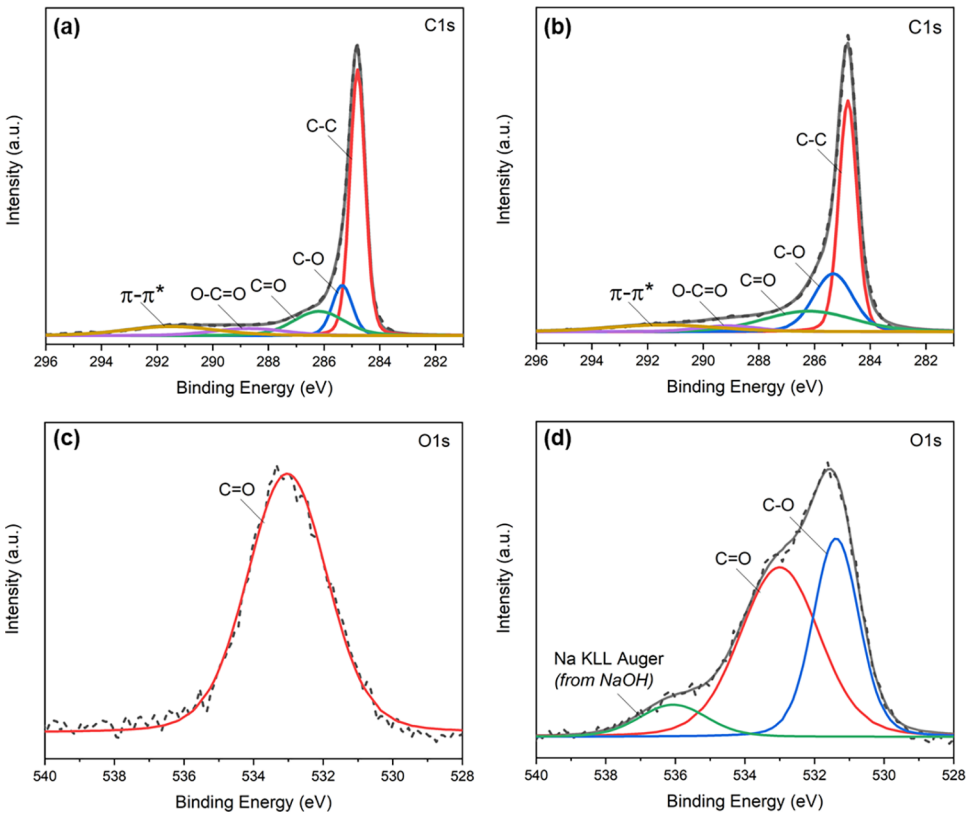

Figure 3. XPS characterization of pristine and anodized LIG electrodes: C 1s spectra of the pristine LIG electrode (a). C 1s spectra of the anodized LIG electrode (b). O 1s spectra of the pristine LIG electrode (c). O 1s spectra of the anodized LIG electrode (d).

3. RESULTS AND DISCUSSION

3.1. Characterization of Fabricated LIG/PB−CS Electrodes. *3.1.1. Raman Characterization.* Raman spectroscopy helped confirm the laser-induced graphitization of PI, subsequent functionalization of LIG in the alkaline solution, and its hybridization with PB−CS. The presence of graphene in LIG was established via the appearance of characteristic D, G, and two-dimensional (2D) bands located at 1344, 1582, and 2687 cm^{-1}, respectively, shown in Figure 2A.[42,47] The D band, representative of the disordered graphitic structure, originates from the stretching vibration of sp^3 hybridized carbon atoms at the edge or basal planes of graphene sheets.[48,49] The high I_D/I_G ratio in the pristine LIG of 0.79 ± 0.05 is indicative of a large concentration of defects, corroborated by the highly porous and weblike morphology observed by SEM (Figure S5A). Different from a perfect lattice surface, defective sites are particularly important to electrochemical functionalization reactions, where they can bind to reaction intermediates as in the case of the anodization process carried out here. The 2D peak is generated by a two-phonon, second-order intervalley scatter.[50] The presence of a 2D band at 2700 cm^{-1} reveals successful graphitization of the PI, whereas a full width at half-maximum (FWHM) greater than 70 cm^{-1} (90.8 cm^{-1}) is indicative of a three-dimensional morphology of graphene layers randomly stacked in the *c*-axis.[42,51] The I_{2D}/I_G value of 0.94 ± 0.17 implies the presence of multilayer graphene. Anodization of LIG (Figure 2A) caused a rise in the I_D/I_G ratio (1.08 ± 0.02) due to an increase of oxygen functional groups (defects), which allowed D peak activation. Furthermore, this increase in oxygen groups was accompanied by a broadening of 2D FWHM (97.7 cm^{-1}) and a decrease of the I_{2D}/I_G intensity ratio (0.59 ± 0.09).[52] The enhancement in oxygen groups was accompanied by an increased hydrophilicity and improved electrochemical performance as discussed later.

The development of peaks at 217 and 276 cm^{-1} on the PB−CS-coated LIG, as shown in Figure 2B, is ascribed to FeCNFe vibrations and indicates the presence of Prussian blue.[53−55] However, the assignment of low-frequency bands (<300 cm^{-1}) has rarely been reported in the literature. The peaks at 2099 and 2150 cm^{-1} on the PB−CS-coated electrodes are attributed to asymmetric and symmetric stretch vibrations of Fe^{II}−C≡N−Fe^{III}, respectively (Figure S3).[56−59] The frequency of the cyanide vibration stretching mode, ν(C≡N), is sensitive to the oxidation state of the coordinating iron, with previous studies showing that ν(C≡N) coordinated to Fe^{3+} displays higher wavenumber peaks than that with Fe^{2+}.[58,59] The two Raman peaks located at 2099 and 2150 cm^{-1} confirm the coexistence of Fe^{2+} and Fe^{3+}, which is in agreement with our XPS results. The characteristic PB peaks at 217 and 276 cm^{-1} are present on the PB−CS-coated electrodes following deposition and are maintained following the activation of CVs in the KCl supporting electrolyte and 60 min heat treatment at 100 °C. The stretching vibrations of Fe^{II}−C≡N−Fe^{III} are the most prevalent in spectra from electrodes that received both postdeposition treatments (CVs in KCl and heat treatment), suggesting that these modifications serve to improve the crystallinity of the coating (Figure S4). Repeated CVs in the supporting electrolyte, which included HCl, ensured that no hydroxide ions were present within the coordination spheres of the ferrous ions.[32] This, combined with the heat treatment step, is typically described in the literature as serving to stabilize the PB coating.

https://doi.org/10.1021/acsanm.3c01199
ACS Appl. Nano Mater. XXXX, XXX, XXX−XXX

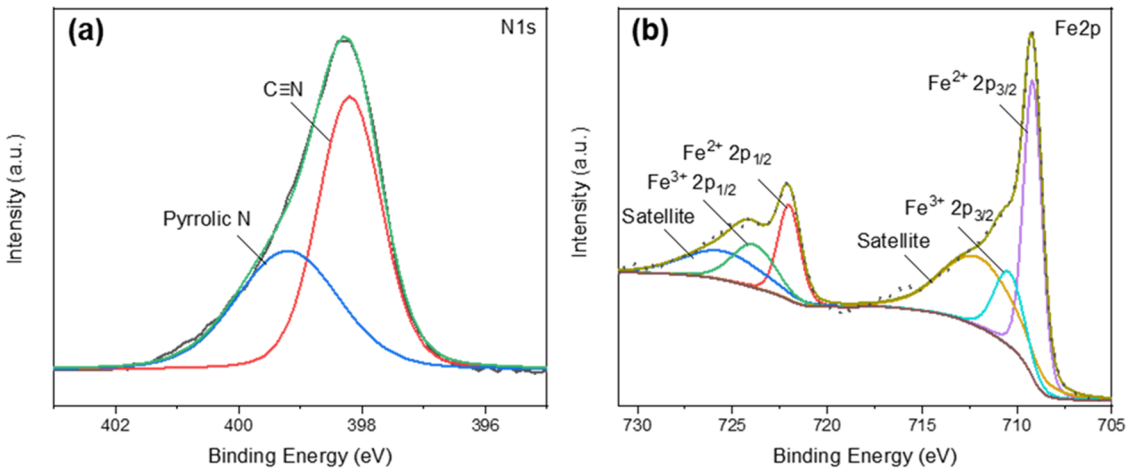

Figure 4. N 1s and Fe 2p regions of the PB−CS-coated electrode. High-resolution XPS of N 1s (a) and Fe 2p (b) regions on the PB−CS-coated LIG electrode.

3.1.2. SEM Characterization. By the addition of chitosan to the Prussian blue (PB) precursor in the deposition solution, the resulting PB−CS coating on LIG was found to consist of PB nanoparticles (around 50−100 nm in diameter) encapsulated within a thin matrix/network of CS, evenly distributed across the electrode surface (Figure S5B). The thickness of the electroactive LIG/PB−CS layer was found to be ∼20 μm as found from an SEM cross section (Figure S6). The presence of numerous PB nanoparticles with nanometer dimensions in the PB−CS coating denotes a high density of nucleation sites, which is related to the electrodeposition deposition conditions (for example, applied voltage, precursor concentration, deposition time). EDS displayed larger counts attributed to potassium (Kα) and iron (Kα and Lα) on the PB−CS-coated electrode, corroborating the fact that hybridization of PB with CS in a one-step deposition increased the quantity of Prussian blue coating retained on the electrode after deposition (Figure S7).

3.1.3. XPS Characterization. The elemental characterization of LIG/PB−CS electrodes, at each step of the fabrication process, was performed via X-ray photoelectron spectroscopy (XPS). Figure S8 presents the survey spectra after each step of electrode preparation, whereas the calculated atomic percentage concentration of relevant elements is presented in Table S1. Wide survey scan of pristine and anodized LIG demonstrated the presence of C and O at binding energies around 285 and 533 eV, respectively (Figure S8). In addition to these elements, the presence of a small amount of Na element (Na KL1) at 497 eV could be observed in anodized LIG, originating from the NaOH electrolyte used in the anodization process. It is worth mentioning that the absence of the N 1s peak from LIG spectra indicates that any nitrogen groups within the polyimide have been successfully removed by its photothermal conversion to graphitic surface layers. The atomic percentage concentration of oxygen in pristine LIG (3.25%) was less than that detected in the anodized sample (7.27%), demonstrating the successful addition of oxygen functionalities by anodization in alkaline media in corroboration with the Raman analysis. Figure 3 presents the C 1s and O 1s core-level spectra of pristine and anodized LIG electrodes, respectively. Calculated from the integrated areas of respective high-resolution XPS spectra, the stoichiometric ratio of C to O was found to decrease (from 6.96 for pristine to 4.75 for anodized LIG) after anodization in the alkaline solution, demonstrating the expected increase in oxygen groups in agreement with previous anodization studies in fibrous carbon electrodes.[60] The C 1s XPS spectra (Figure 3A,B) show peaks at 285.3, 286.2, and 289.1 eV attributed to C−O, C═O, and O−C═O bonding configurations, respectively. Comparison of the deconvoluted C 1s peaks obtained from pristine and anodized LIG (Figure 3A,B) revealed an increase in oxygen functionalities, particularly in C−O bonds.

Increased oxygen functionalities introduced to pristine LIG by anodization were also evidenced by the O 1s spectra. Pristine LIG demonstrates a dominance of C═O bonds at 533.0 eV due to ketone or carbonyl functional groups (Figure 3C). In contrast, the O 1s spectrum obtained from the anodized sample requires multiple peak fittings due to the introduction of a large C−O contribution at 531.4 eV (Figure 3D). This large C−O contribution due to phenol groups after anodization is in agreement with the C 1s spectra, where an enhanced C−O contribution was evident.

The electrochemical deposition of Prussian blue, in its pure (PB only) or hybridized form with chitosan (PB−CS), was confirmed by survey spectra, which displayed the presence of N and Fe at binding energies around 398.4 and 709.8 eV, respectively, as shown in Figure S8. Surprisingly, the atomic concentration of iron in the PB−CS hybrid (4.52 atom %) was higher than that of pure PB (2.03 atom %). This raise in iron content can be explained bearing in mind that PB is unstable in neutral solutions, leading to considerable PB removal upon rinsing of the coated electrode in water following deposition to remove weakly adsorbed PB.

The high-resolution N 1s spectra of the PB−CS-coated LIG were fitted with two peak components located at 399.3 and 398.1 eV and are attributed to pyrrolic and C≡N groups, respectively (Figure 4A).[61,62] The latter peak at 398.1 eV is associated with the ferrocyanide component of Prussian blue, which contains an abundance of C≡N bonds.

A high-resolution spectrum of the Fe 2p region from the PB−CS-coated electrode demonstrates the classic iron asymmetric peaks with a doublet pair, indicating that both the Fe^{2+} and Fe^{3+} states are present within the deposited coating (Figure 4B). Fitting of this spectrum reveals that peaks for Fe^{2+} $2p_{1/2}$ and Fe^{2+} $2p_{3/2}$ are present at binding energies of 722.01 and 709.16 eV, respectively. The peaks at binding

https://doi.org/10.1021/acsanm.3c01199
ACS Appl. Nano Mater. XXXX, XXX, XXX−XXX

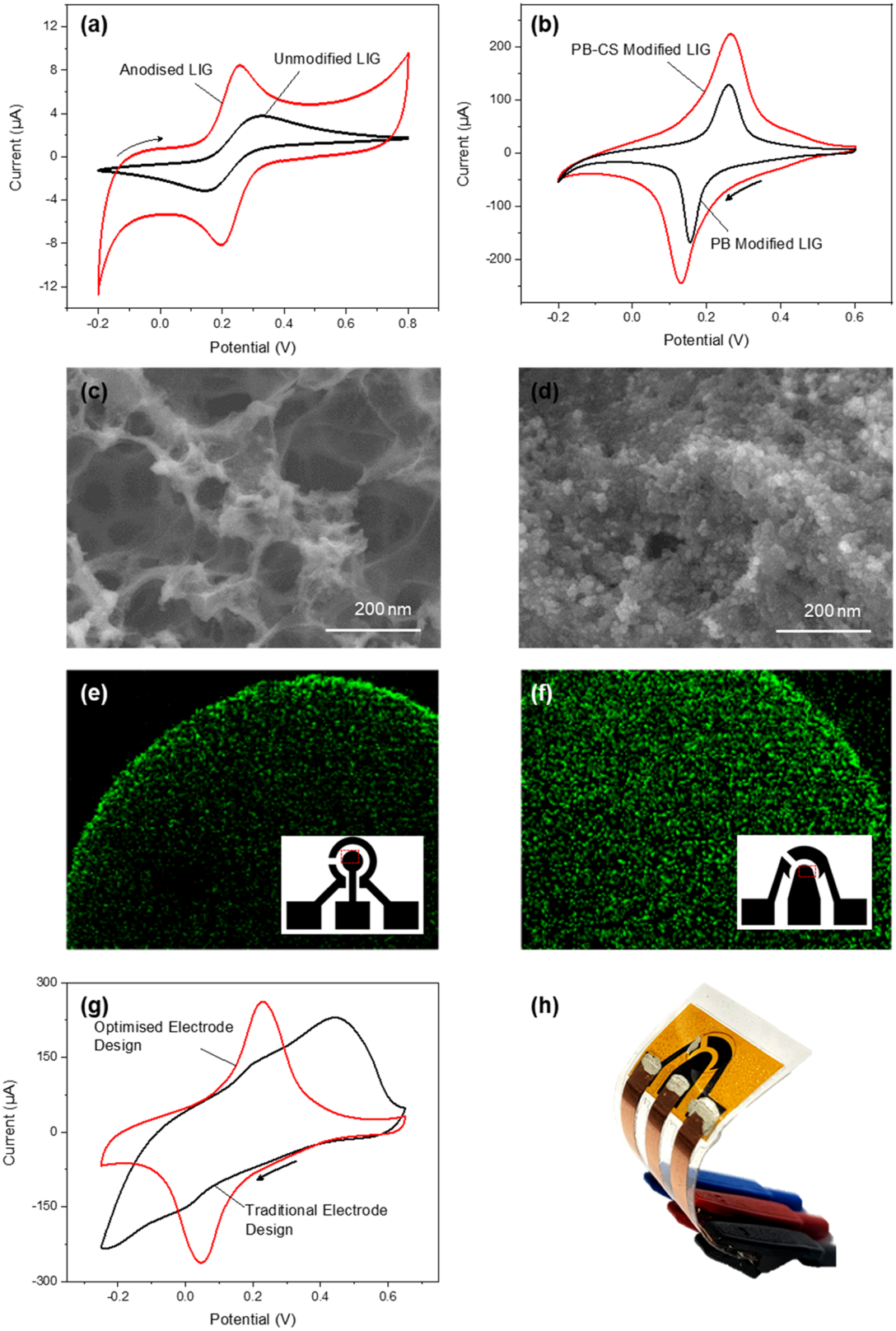

Figure 5. Effect of electrode fabrication steps on the morphology and electrochemical performance of the integrated flexible sensor. CVs of pristine LIG (black) and anodized LIG (red) electrodes toward 2 mM ferrocyanide (a). CVs of the PB-modified single LIG electrode (black) compared to the PB−CS-modified single LIG electrode (red) in a pH 6 Britton−Robinson buffer (b). SEM of PB coating on LIG (c). SEM of PB−CS-coated LIG, showing a homogeneous coating (d). EDS mapping of the working electrode of an integrated electrode showing the Fe Kα (green) signal on the working electrode that has been patterned in a traditional three-electrode configuration (overlayed) after PB−CS deposition (e). EDS mapping of the working electrode of an integrated electrode using the optimized working electrode design (overlayed) after PB−CS deposition (f). CVs in 0.1 M KCl of traditional (black) and optimized (red) integrated sensors (g). Integrated electrode encased in a flexible laminate with an aperture defining the working area (h).

https://doi.org/10.1021/acsanm.3c01199
ACS Appl. Nano Mater. XXXX, XXX, XXX−XXX

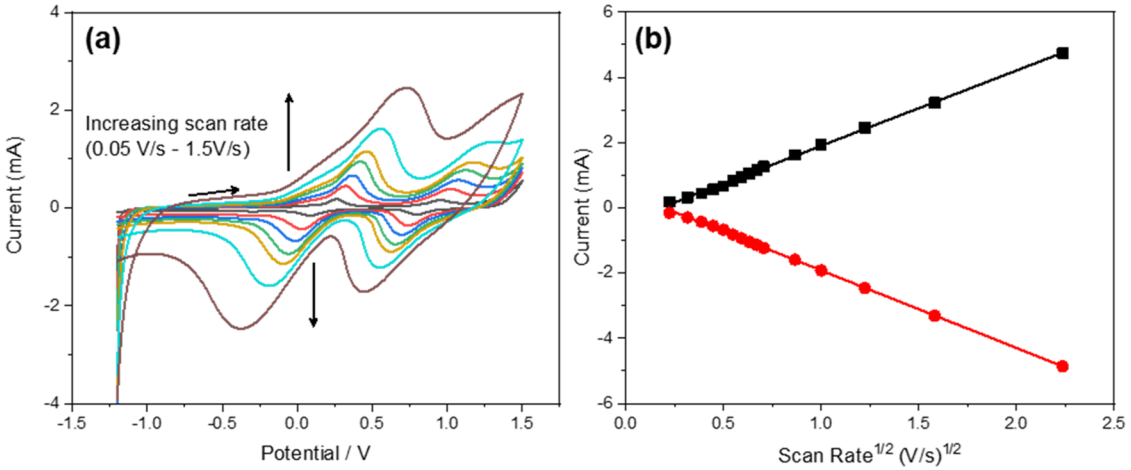

Figure 6. Effect of scan rate on the peak heights of cyclic voltammograms in the buffer. CV scans of the LIG/PB−CS electrode in a buffer at increasing scan rates (a). Anodic (I_{PA}) and cathodic (I_{PC}) peak currents of the PW-to-PB couple plotted against square root of the scan rate (b).

energies of 723.87 and 710.43 eV are assigned to Fe^{3+} $2p_{1/2}$ and Fe^{3+} $2p_{3/2}$, respectively, with their adjacent satellite peaks at 725.50 and 712.00 eV.[63,64] The relative concentration of Fe^{2+} to Fe^{3+} was estimated as 1.88 based on integration of relevant peaks. The Fe 2p spectrum of the control PB-coated electrode (without the chitosan component) demonstrates a similar envelope to the PB−CS. However, the intensity is considerably reduced for both Fe^{2+} and Fe^{3+} states, indicating that a higher quantity of iron is maintained on the electrode surface when chitosan is included in the deposition solution, which is in agreement with the EDS results (Figure S7). Similarly, the stoichiometric ratio of C to Fe decreased from 1.24 (PB) to 0.51 (PB−CS) with the inclusion of chitosan within the deposition solution, demonstrating the stabilizing role of chitosan on preserving PB.

3.2. Electrochemical Characterization and Translation to the Fully Integrated Sensor. Preliminary work in PB−CS sensor characterization was carried out using a single (nonintegrated) LIG/PB−CS working electrode in a standard three-electrode setup by examining the effect of scan rate on cyclic voltammograms and elucidating the diffusion-controlled process.

The as-synthesized (pristine) LIG is not suitable for electrochemical sensing due to its hydrophobic surface. For a hydrophobic surface, the electrolyte solution cannot reach all parts of the electrode such as nanopores; as a result, these parts do not contribute to the sensing signal, and hence, the overall sensitivity is reduced. Application of a positive voltage for a few seconds induced controlled chemical modification on the surface of laser-induced graphene of desired wettability while maintaining its conductive properties. Anodization in alkaline media of the pristine LIG electrode was found to reduce the anodic−cathodic peak separation (ΔE_p from 0.1825 to 0.0595 V) using a ferrocyanide inner-sphere mediator (Figure 5A). This inner-sphere redox probe is highly sensitive to the nature of the electrode surface. The reduced ΔE_p peak separation indicates that enhanced electron-transfer kinetics were induced by the anodization treatment. One reason for the improved performance is related to the improved hydrophilicity of the LIG electrode imparted by the oxygen functional groups. Similar improvements in electron-transfer kinetics have been observed after anodization of glassy carbon[65] and carbon fiber electrodes.[60] The anodization process facilitates enhanced intercalation of redox ions within the pores of LIG, leading to a higher capacitance, as evidenced by the increased area enclosed within the CV curves. The anodization surface treatment was further exploited to prevent the innate hydrophobic behavior of pristine LIG from acting as a barrier to the uniform electrodeposition of PB−CS coating. The PB−CS-coated LIG (Figure 5D) demonstrated a homogeneous covering on the electrode surface compared to the sparsely PB-coated electrode (Figure 5C). This was reflected by the larger intensity of cathodic (45.64% increase) and anodic peaks achieved by the PB−CS electrode on CV in pH 6 buffer compared to the PB electrode (Figure 5B). Repeated exposure to neutral solutions is typical of an electrode in a wearable biosensor application. Therefore, hybridizing the deposition of Prussian blue with chitosan shows advantage as the coating remains on the electrode surface throughout the postdeposition treatment and dH_2O rinsing steps. This improved coverage promises a greater availability of the PB for the catalysis of H_2O_2 in a sensing application.

The single LIG/PB−CS working electrode was translated to an integrated sensor by optimizing the three-electrode configuration through an iterative design process. Using the traditional electrode design optimized for drop-casting of coatings (inset of Figure 5E), EDS mapping revealed that the majority of the characteristic Fe Kα signal in the hybrid PB−CS coating was concentrated around the circumference of the circular electrode (Figure 5E), with a considerably reduced signal in the center, revealing a nonuniform coating. However, by maintaining the same electrode working area, while increasing the width of the neck portion, the Fe Kα signal from the electrochemically deposited coating became consistent across the working electrode, suggesting a uniform PB−CS deposition (Figure 5F). This improved coating in the optimized electrode design yielded a reversible behavior during CVs in a 0.1 M KCl solution, suggesting better electron-transfer kinetics (Figure 5G). This optimized design and the coating parameters were used to assemble the final integrated electrode (Figure 5H) and were used for all electrochemical tests toward H_2O_2 sensing.

3.3. Electrochemical Characterization of the LIG/PB−CS H_2O_2 Sensor. Cyclic voltammograms (CVs) of the LIG/PB−CS-coated electrodes were completed in a pH 7 Britton−Robinson buffer solution at increasing scan rates in the range

https://doi.org/10.1021/acsanm.3c01199
ACS Appl. Nano Mater. XXXX, XXX, XXX−XXX

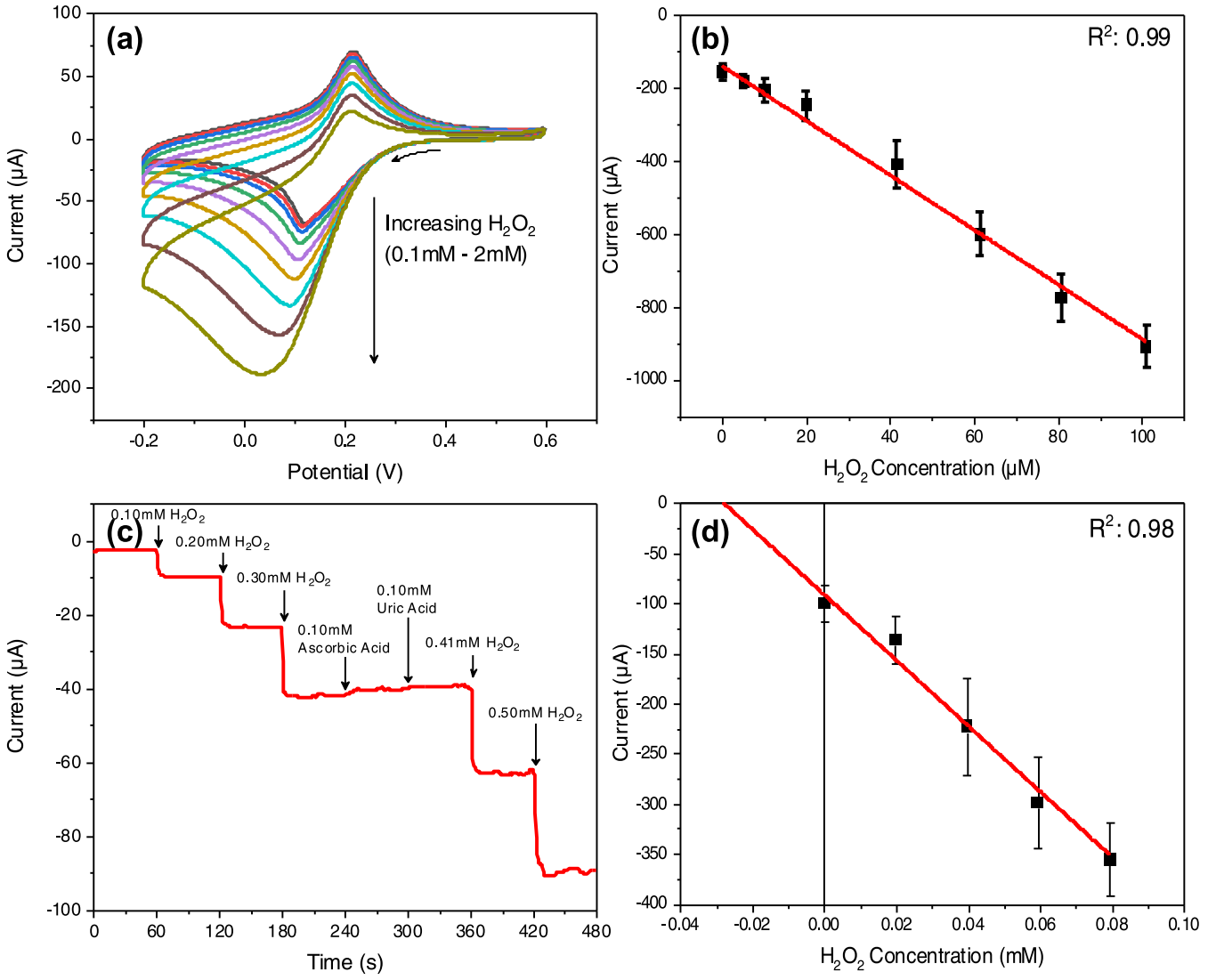

Figure 7. Sensitivity and specificity of the integrated LIG\PB−CS electrochemical sensor. CV scans of the LIG/PB−CS electrode in the buffer with increasing concentration of H_2O_2 (a). Calibration curve using chronoamperometry data for n = 3 LIG/PB−CS integrated sensors (b). Continuous chronoamperometry of the integrated sensor at −0.036 V (vs Ag/AgCl) with standard additions of H_2O_2 and interfering species (AA and UA); arrows show the cell concentration (c). Recovery protocol using a 25 μM H_2O_2 spike (n = 3) demonstrating a recovery of 100.1% (d).

of 0.05−5 V/s from −1.2 to +1.5 V (Figure 6A). The peak heights of the PB-to-PW redox couple (eq 1a) demonstrated a linear relationship with square root of the scan rate (Figure 6B). This reveals a diffusion-controlled process, facilitated by movement of potassium ions through the PB−CS coating, indicating the suitability of the PB−CS coating for application in a quantitative sensor.[66,67] The potentials of the anodic and cathodic peaks shift outward with increasing scan rate, implying a quasi-reversible behavior.[68]

All H_2O_2 sensitivity experiments presented were completed using an integrated sensor to demonstrate the application of LIG functionalized with a PB−CS hybrid coating as a wearable skin sweat sensor. Initially, the response of the integrated sensor to H_2O_2 detection was characterized by cyclic voltammetry. Scans were taken from +0.6 to −0.2 V in increasing concentrations of H_2O_2 in a pH 6 BR buffer; this value was selected to reflect the near-neutral pH of eccrine sweat. The cathodic current around 0 V on the negative sweep increased linearly with increasing H_2O_2 concentration proving the catalytic behavior of the PB−CS coating (Figure 7A). The current from the cathodic sweep of cyclic voltammograms with increasing concentrations of H_2O_2 was examined to select the optimal potential for amperometric detection. A potential of −0.036 vs Ag/AgCl was used for chronoamperometry measurements and achieved a detection limit of 6.31 μM. This was calculated ((3.3 × standard deviation of the blank)/slope) from three replicates of chronoamperometric measurements at −0.036 V (Figure S9A), using current values taken from early in the chronoamperometry measurements, and was linear (R^2: 0.99) up to 100 μm (Figure 7B). To achieve a wide linear range, the sampling point from three replicates of chronoamperometry was increased to 1.6 s. The resulting calibration plot from this time point (Figure S9B) has a reduced slope compared to that in Figure 7B; however, the fit is linear to 1000 μM (R^2: 0.996). The integrated sensor demonstrated a rapid response to multiple additions of H_2O_2 in a stirred buffer solution (Figure 7C). The small negative potential used during H_2O_2 detection prevented interfering current from the reduction of dissolved oxygen in solution. Therefore, no degassing step was required, validating this

https://doi.org/10.1021/acsanm.3c01199
ACS Appl. Nano Mater. XXXX, XXX, XXX−XXX

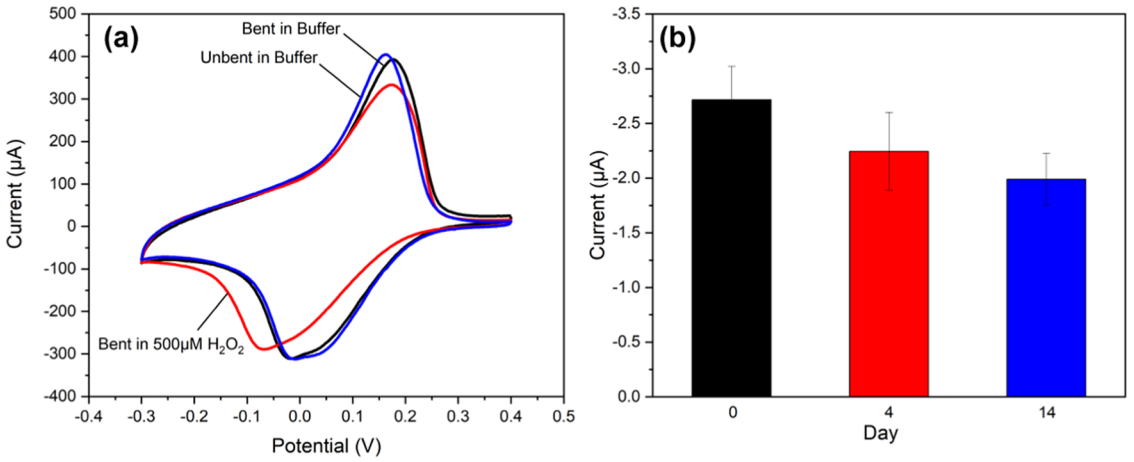

Figure 8. Mechanical and time stability of LIG and PB−CS. CVs of the LIG/PB−CS integrated electrode in the pH 6 Britton−Robinson buffer before and after application of 11 mm bending radius and following the addition of H_2O_2 (a). Response of LIG/PB−CS integrated electrodes to 100 μM H_2O_2 after 4 and 14 days of storage (b).

detection mechanism for use in a skin biosensor. The response to H_2O_2 during chronoamperometry was found to be largely unaffected by the addition of common electrochemical interferents (uric acid and ascorbic acid) to the cell. Additionally, their presence in solution did not impact the performance of the sensor during subsequent additions of H_2O_2, proving the specificity of the integrated sensor to H_2O_2 (Figure 7C). We also employed chronoamperometry to quantify the concentration of H_2O_2 within a complex simulated biofluid. The described hybridized deposition of PB with CS and the optimized electrode geometries of the integrated electrode achieved a notable detection limit of 6.31 μM and maintained this response over 14 days (Figure 8B). The simultaneous incorporation of chitosan, a natural polymer insoluble at neutral pH, into the deposition solution was crucial in achieving a stable electrode response toward H_2O_2. Moreover, this sensor was highly specific toward the target analyte and immune to interference from dissolved oxygen in solution and common electrochemical interferents. The work presented here provides a detailed comprehensive study on the optimization of an integrated LIG electrode with a one-step electrodeposition of a PB−CS hybrid coating.

Chronoamperometry was further used to investigate the suitability of the LIG/PB−CS integrated electrode for detecting the presence of H_2O_2 in sweat. A percentage recovery protocol in a small volume of fortified artificial eccrine perspiration (AEP) using a 25 μM spike of H_2O_2 revealed a recovery of 100.1% in triplicate analyses (Figure 7D). No dilution or adjustments of the AEP were required to achieve the reported results. This commercial sample comprised the major amino acids, minerals, and metabolites present in sweat and was not found to be detrimental to the operation of the sensor, which demonstrated interference-free measurement. Considering these findings and the facile fabrication of a flexible electrode substrate, we propose this detection mechanism and method as the basis for any skin-attached oxidase enzymatic biosensor.

The same recovery protocol was used to characterize the response of the sensor to H_2O_2 in human eccrine sweat; the initial spike was added to 400 μL of unmodified sweat, and the response was recorded. Regression showed that this 25 μM was recovered in three sweat samples as shown in Table 1. A different integrated electrode was used for each recovery experiment in the three human sweat samples, resulting in the observed variance in the gradient.

Table 1. Summary of Recovery Results Achieved by the LIG/PB−CS H_2O_2 Integrated Sensor in Unmodified Human Eccrine Perspiration

sex of participant	age of participant	H_2O_2 recovery (%)	gradient (μA mM $^{-1}$)
female	21	98.40	−57.09
male	42	99.70	−42.40
male	33	98.10	−67.13

The detection limit and linear range of the developed system are competitive with previously demonstrated Prussian blue sensors on rigid substrates[10−16] presented in Table S2, thereby demonstrating the suitability of the substrate. Although other reports in the table using LIG achieve a lower detection limit (e.g., LIG/Cu−Ru and LIG-PtNPs), these employ various metallic nanoparticle coatings, which require larger negative detection potentials.[20,21] The reduction of dissolved oxygen in solution necessitated deaeration of the test solution with nitrogen to achieve interference-free detection. Although the LIG/AgNP sensor displays a lower detection limit, its fabrication is based on noble metals and its detection range is limited in the 10−50 μM region. The LIG/PB−CS sensor of this work demonstrates superb sensitivity in complex biological solutions compared to other flexible systems with more complex, costly, and manually intensive manufacturing.[17−19,22]

3.4. Suitability of the LIG/PB−CS H_2O_2 Sensor for Use in a Wearable Application. Mechanical bending of the fabricated LIG material demonstrated that application of an 11 mm bending radius did not have a detrimental effect on the reversibility or peak height of the PB−CS integrated sensor, and its response toward H_2O_2 was maintained (Figure 8A). On repeated CV scans in the bent state at 30 min intervals (Figure S10A), the response to H_2O_2 by the integrated electrode was maintained (Figure S10B). To investigate the lifetime of the developed sensor, the amperometric response of the integrated electrodes in the buffer was recorded 4 and 14 days after manufacture (Figure 8B). It was found that the integrated reference electrode was stable and the overall sensor retained 82.6% of its original current density toward 100 μM H_2O_2 after

https://doi.org/10.1021/acsanm.3c01199
ACS Appl. Nano Mater. XXXX, XXX, XXX−XXX

4 days of storage at 4 °C. This decreased slightly to 73.2% on day 14, suggesting that the PB−CS coating has good stability.

4. CONCLUSIONS

In summary, we have successfully developed a stable, surface-engineered LIG/PB−CS integrated flexible amperometric sensor for the sensitive detection of H_2O_2 in sweat. The crucial steps involved the proper electrodeposition of a Prussian blue (PB)−chitosan (CS) network and the appropriate design of the integrated sensor configuration were optimized by concurrent feedback from electrochemical and morphological characterization activities. Amperometric peroxide biosensing over a wide linear range (10−1000 μM) with a low detection limit of 6.31 μM at near-zero detection potential and a recovery of 98.73% in human eccrine perspiration was achieved. The near-zero detection potential ensured high specificity, immunity from oxygen reduction, and common interfering species. Importantly, the inclusion of CS in the hybrid PB−CS coating facilitated high stability in a complex biological solution such as sweat. The sensor encompasses the benefits of using LIG as a base electrode, namely, flexibility and the ability to rapidly manufacture complex geometries. This, combined with the facile functionalization of the working electrode by the one-step electrochemical deposition of the low-cost catalytic (PB) and stabilizing biocompatible (CS) agents, makes the sensor amenable to large-scale manufacture, enhancing its chances for future commercialization. The resulting flexible sensor is simple to operate, and its underpinning configuration is suitable for use in common oxidase enzyme (glucose, bilirubin, lactate) detection. All of these attributes (relative ease of manufacturing, flexibility, biocompatibility, appropriate linear range, and specificity in human sweat) make our sensor a compelling contender for continuous monitoring of metabolites on-skin. Future work would involve the development of a microfluidic platform and miniaturization of the electronic system toward the realization of real-time continuous monitoring of sweat metabolites in human participants.

■ ASSOCIATED CONTENT

Supporting Information

The Supporting Information is available free of charge at https://pubs.acs.org/doi/10.1021/acsanm.3c01199.

> Cyclic voltammograms of an integrated LIG electrode; schematic of the acrylic electrochemical cell; Raman spectra, SEM images, and EDS and XPS spectra of PB−CS LIG electrodes; summary table with XPS atomic concentrations of all electrodes; chronoamperometry data and calibration curve; electrochemical stability of integrated LIG sensors; and summary comparison table of main parameters from the reported literature (PDF)

■ AUTHOR INFORMATION

Corresponding Author

Pagona Papakonstantinou − *School of Engineering, Nanotechnology & Integrated Bio-Engineering Centre (NIBEC), Ulster University, Belfast BT15 1AP, U.K.;* orcid.org/0000-0003-0019-3247; Email: p.papakonstantinou@ulster.ac.uk

Authors

Robert Barber − *School of Engineering, Nanotechnology & Integrated Bio-Engineering Centre (NIBEC), Ulster University, Belfast BT15 1AP, U.K.;* orcid.org/0000-0002-4762-1918

James Davis − *School of Engineering, Nanotechnology & Integrated Bio-Engineering Centre (NIBEC), Ulster University, Belfast BT15 1AP, U.K.;* orcid.org/0000-0003-4284-4431

Complete contact information is available at: https://pubs.acs.org/10.1021/acsanm.3c01199

Funding

The Department for the Economy (DfE) Northern Ireland and Abbott Diabetes Care Inc.

Notes

The authors declare no competing financial interest.

■ ACKNOWLEDGMENTS

The authors acknowledge financial support from the Department for the Economy (DfE) Northern Ireland and Abbott Diabetes Care Inc.

■ REFERENCES

(1) Low, J. A.; Toh, H. J.; Tan, L. L. C.; Chia, J. W. K.; Soek, A. T. S. The Nuts and Bolts of Utilizing Telemedicine in Nursing Homes − The GeriCare@North Experience. *J. Am. Med. Dir. Assoc.* **2020**, *21*, 1073−1078.

(2) Yu, Z.; Tang, Y.; Cai, G.; Ren, R.; Tang, D. Paper Electrode-Based Flexible Pressure Sensor for Point-of-Care Immunoassay with Digital Multimeter. *Anal. Chem.* **2019**, *91*, 1222−1226.

(3) Yu, Z.; Tang, D. Artificial Neural Network-Assisted Wearable Flexible Sweat Patch for Drug Management in Parkinson's Patients Based on Vacancy-Engineered Processing of g-C 3 N 4. *Anal. Chem.* **2022**, *94*, 18000−18008.

(4) Yu, Z.; Gong, H.; Xue, F.; Zeng, Y.; Liu, X.; Tang, D. Flexible and High-Throughput Photothermal Biosensors for Rapid Screening of Acute Myocardial Infarction Using Thermochromic Paper-Based Image Analysis. *Anal. Chem.* **2022**, *94*, 13233−13242.

(5) Heikenfeld, J.; Jajack, A.; Feldman, B.; Granger, S. W.; Gaitonde, S.; Begtrup, G.; Katchman, B. A. Accessing Analytes in Biofluids for Peripheral Biochemical Monitoring. *Nat. Biotechnol.* **2019**, *37*, 407−419.

(6) Chung, M.; Fortunato, G.; Radacsi, N. Wearable Flexible Sweat Sensors for Healthcare Monitoring: A Review. *J. R. Soc., Interface* **2019**, *16*, No. 20190217.

(7) Wei, X.; Zhu, M.; Li, J.; Liu, L.; Yu, J.; Li, Z.; Ding, B. Wearable Biosensor for Sensitive Detection of Uric Acid in Artificial Sweat Enabled by a Fiber Structured Sensing Interface. *Nano Energy* **2021**, *85*, No. 106031.

(8) Zhu, M.; Li, J.; Yu, J.; Li, Z.; Ding, B. Superstable and Intrinsically Self-Healing Fibrous Membrane with Bionic Confined Protective Structure for Breathable Electronic Skin. *Angew. Chem., Int. Ed.* **2022**, *61*, No. e202200226.

(9) Cai, S.; Xu, C.; Jiang, D.; Yuan, M.; Zhang, Q.; Li, Z.; Wang, Y. Air-Permeable Electrode for Highly Sensitive and Noninvasive Glucose Monitoring Enabled by Graphene Fiber Fabrics. *Nano Energy* **2022**, *93*, No. 106904.

(10) Karyakin, A. A.; Karyakina, E. E. Prussian Blue-Based "artificial Peroxidase" as a Transducer for Hydrogen Peroxide Detection. Application to Biosensors. *Sens. Actuators, B* **1999**, *57*, 268−273.

(11) O'Halloran, M. P.; Pravda, M.; Guilbault, G. G. Prussian Blue Bulk Modified Screen-Printed Electrodes for H2O2 Detection and for Biosensors. *Talanta* **2001**, *55*, 605−611.

(12) Pires, B. M.; Galdino, F. E.; Bonacin, J. A. Electrocatalytic Reduction of Oxygen by Metal Coordination Polymers Produced

from Pentacyanidoferrate(II) Complex. *Inorg. Chim. Acta* **2017**, *466*, 166−173.
(13) Nossol, E.; Zarbin, A. J. G. A Simple and Innovative Route to Prepare a Novel Carbon Nanotube/Prussian Blue Electrode and Its Utilization as a Highly Sensitive H 2 O 2 Amperometric Sensor. *Adv. Funct. Mater.* **2009**, *19*, 3980−3986.
(14) Cao, L.; Liu, Y.; Zhang, B.; Lu, L. In Situ Controllable Growth of Prussian Blue Nanocubes on Reduced Graphene Oxide: Facile Synthesis and Their Application as Enhanced Nanoelectrocatalyst for H2O2 Reduction. *ACS Appl. Mater. Interfaces* **2010**, *2*, 2339−2346.
(15) Zhang, Y.; Sun, X.; Zhu, L.; Shen, H.; Jia, N. Electrochemical Sensing Based on Graphene Oxide/Prussian Blue Hybrid Film Modified Electrode. *Electrochim. Acta* **2011**, *56*, 1239−1245.
(16) Katic, V.; dos Santos, P. L.; dos Santos, M. F.; Pires, B. M.; Loureiro, H. C.; Lima, A. P.; Queiroz, J. C. M.; Landers, R.; Muñoz, R. A. A.; Bonacin, J. A. 3D Printed Graphene Electrodes Modified with Prussian Blue: Emerging Electrochemical Sensing Platform for Peroxide Detection. *ACS Appl. Mater. Interfaces* **2019**, *11*, 35068−35078.
(17) Settu, K.; Lai, Y.-C.; Liao, C.-T. Carbon Nanotube Modified Laser-Induced Graphene Electrode for Hydrogen Peroxide Sensing. *Mater. Lett.* **2021**, *300*, No. 130106.
(18) Zhao, G.; Wang, F.; Zhang, Y.; Sui, Y.; Liu, P.; Zhang, Z.; Xu, C.; Yang, C. High-Performance Hydrogen Peroxide Micro-Sensors Based on Laser-Induced Fabrication of Graphene@Ag Electrodes. *Appl. Surf. Sci.* **2021**, *565*, No. 150565.
(19) Aparicio-Martínez, E.; Ibarra, A.; Estrada-Moreno, I. A.; Osuna, V.; Dominguez, R. B. Flexible Electrochemical Sensor Based on Laser Scribed Graphene/Ag Nanoparticles for Non-Enzymatic Hydrogen Peroxide Detection. *Sens. Actuators, B* **2019**, *301*, No. 127101.
(20) Thirumalai, D.; Lee, J. U.; Choi, H.; Kim, M.; Lee, J.; Kim, S.; Shin, B. S.; Chang, S. C. In Situsynthesis of Copper-Ruthenium Bimetallic Nanoparticles on Laser-Induced Graphene as a Peroxidase Mimic. *Chem. Commun.* **2021**, *57*, 1947−1950.
(21) Zhang, Y.; Zhu, H.; Sun, P.; Sun, C.; Huang, H.; Guan, S.; Liu, H.; Zhang, H.; Zhang, C.; Qin, K. Laser-induced Graphene-based Non-enzymatic Sensor for Detection of Hydrogen Peroxide. *Electroanalysis* **2019**, *31*, 1334−1341.
(22) Bauer, M.; Wunderlich, L.; Weinzierl, F.; Lei, Y.; Duerkop, A.; Alshareef, H. N.; Baeumner, A. J. Electrochemical Multi-Analyte Point-of-Care Perspiration Sensors Using on-Chip Three-Dimensional Graphene Electrodes. *Anal. Bioanal. Chem.* **2021**, *413*, 763−777.
(23) Sies, H. Hydrogen Peroxide as a Central Redox Signaling Molecule in Physiological Oxidative Stress: Oxidative Eustress. *Redox Biol.* **2017**, *11*, 613−619.
(24) Karyakin, A. A. Advances of Prussian Blue and Its Analogues in (Bio)Sensors. *Curr. Opin. Electrochem.* **2017**, *5*, 92−98.
(25) Maji, S. K.; Sreejith, S.; Mandal, A. K.; Ma, X.; Zhao, Y. Immobilizing Gold Nanoparticles in Mesoporous Silica Covered Reduced Graphene Oxide: A Hybrid Material for Cancer Cell Detection through Hydrogen Peroxide Sensing. *ACS Appl. Mater. Interfaces* **2014**, *6*, 13648−13656.
(26) Ji, X.; Ren, J.; Ni, R.; Liu, X. A Stable and Controllable Prussian Blue Layer Electrodeposited on Self-Assembled Monolayers for Constructing Highly Sensitive Glucose Biosensor. *Analyst* **2010**, *135*, No. 2092.
(27) Garjonytė, R.; Malinauskas, A. Electrocatalytic Reactions of Hydrogen Peroxide at Carbon Paste Electrodes Modified by Some Metal Hexacyanoferrates. *Sens. Actuators, B* **1998**, *46*, 236−241.
(28) De Mattos, I. L.; Gorton, L.; Ruzgas, T.; Karyakin, A. A. Sensor for Hydrogen Peroxide Based on Prussian Blue Modified Electrode: Improvement of the Operational Stability. *Anal. Sci.* **2000**, *16*, 795−798.
(29) Sheng, Q.; Zhang, D.; Shen, Y.; Zheng, J. Synthesis of Hollow Prussian Blue Cubes as an Electrocatalyst for the Reduction of Hydrogen Peroxide. *Front. Mater. Sci.* **2017**, *11*, 147−154.
(30) Yu, Z.; Cai, G.; Ren, R.; Tang, D. A New Enzyme Immunoassay for Alpha-Fetoprotein in a Separate Setup Coupling an Aluminium/Prussian Blue-Based Self-Powered Electrochromic Display with a Digital Multimeter Readout. *Analyst* **2018**, *143*, 2992−2996.
(31) Yu, Z.; Gong, H.; Li, M.; Tang, D. Hollow Prussian Blue Nanozyme-Richened Liposome for Artificial Neural Network-Assisted Multimodal Colorimetric-Photothermal Immunoassay on Smartphone. *Biosens. Bioelectron.* **2022**, *218*, No. 114751.
(32) Karyakin, A. On the Mechanism of H2O2 Reduction at Prussian Blue Modified Electrodes. *Electrochem. Commun.* **1999**, *1*, 78−82.
(33) Yashina, E. I.; Borisova, A. V.; Karyakina, E. E.; Shchegolikhina, O. I.; Vagin, M. Y.; Sakharov, D. A.; Tonevitsky, A. G.; Karyakin, A. A. Sol-Gel Immobilization of Lactate Oxidase from Organic Solvent: Toward the Advanced Lactate Biosensor. *Anal. Chem.* **2010**, *82*, 1601−1604.
(34) Keum, D. H.; Kim, S.-K.; Koo, J.; Lee, G.-H.; Jeon, C.; Mok, J. W.; Mun, B. H.; Lee, K. J.; Kamrani, E.; Joo, C.-K.; Shin, S.; Sim, J.-Y.; Myung, D.; Yun, S. H.; Bao, Z.; Hahn, S. K. Wireless Smart Contact Lens for Diabetic Diagnosis and Therapy. *Sci. Adv.* **2020**, *6*, No. eaba3252.
(35) Haghighi, H.; Licciardello, F.; Fava, P.; Siesler, H. W.; Pulvirenti, A. Recent Advances on Chitosan-Based Films for Sustainable Food Packaging Applications. *Food Packag. Shelf Life* **2020**, *26*, No. 100551.
(36) Ali, A.; Ahmed, S. A Review on Chitosan and Its Nanocomposites in Drug Delivery. *Int. J. Biol. Macromol.* **2018**, *109*, 273−286.
(37) Wang, X.; Gu, H.; Yin, F.; Tu, Y. A Glucose Biosensor Based on Prussian Blue/Chitosan Hybrid Film. *Biosens. Bioelectron.* **2009**, *24*, 1527−1530.
(38) Katas, H.; Wen, C. M. Preparation and Characterisation of Highly Loaded Fluorescent Chitosan Nanoparticles. *ISRN Pharm.* **2011**, *2011*, 1−5.
(39) Chyan, Y.; Ye, R.; Li, Y.; Singh, S. P.; Arnusch, C. J.; Tour, J. M. Laser-Induced Graphene by Multiple Lasing: Toward Electronics on Cloth, Paper, and Food. *ACS Nano* **2018**, *12*, 2176−2183.
(40) Cao, L.; Zhu, S.; Pan, B.; Dai, X.; Zhao, W.; Liu, Y.; Xie, W.; Kuang, Y.; Liu, X. Stable and Durable Laser-Induced Graphene Patterns Embedded in Polymer Substrates. *Carbon* **2020**, *163*, 85−94.
(41) Ye, R.; Chyan, Y.; Zhang, J.; Li, Y.; Han, X.; Kittrell, C.; Tour, J. M. Laser-Induced Graphene Formation on Wood. *Adv. Mater.* **2017**, *29*, No. 1702211.
(42) Lin, J.; Peng, Z.; Liu, Y.; Ruiz-Zepeda, F.; Ye, R.; Samuel, E. L. G. G.; Yacaman, M. J.; Yakobson, B. I.; Tour, J. M. Laser-Induced Porous Graphene Films from Commercial Polymers. *Nat. Commun.* **2014**, *5*, No. 5714.
(43) In, J. B.; Hsia, B.; Yoo, J.-H.; Hyun, S.; Carraro, C.; Maboudian, R.; Grigoropoulos, C. P. Facile Fabrication of Flexible All Solid-State Micro-Supercapacitor by Direct Laser Writing of Porous Carbon in Polyimide. *Carbon* **2015**, *83*, 144−151.
(44) Inagaki, M.; Ohta, N.; Hishiyama, Y. Aromatic Polyimides as Carbon Precursors. *Carbon* **2013**, *61*, 1−21.
(45) Burke, M.; Larrigy, C.; Vaughan, E.; Paterakis, G.; Sygellou, L.; Quinn, A. J.; Herzog, G.; Galiotis, C.; Iacopino, D. Fabrication and Electrochemical Properties of Three-Dimensional (3D) Porous Graphitic and Graphenelike Electrodes Obtained by Low-Cost Direct Laser Writing Methods. *ACS Omega* **2020**, *5*, 1540−1548.
(46) Dutt, J. S. N.; Cardosi, M. F.; Wilkins, S.; Livingstone, C.; Davis, J. Characterisation of Carbon Fibre Composites for Decentralised Biomedical Testing. *Mater. Chem. Phys.* **2006**, *97*, 267−272.
(47) Ferrari, A. C.; Meyer, J. C.; Scardaci, V.; Casiraghi, C.; Lazzeri, M.; Mauri, F.; Piscanec, S.; Jiang, D.; Novoselov, K. S.; Roth, S.; Geim, A. K. Raman Spectrum of Graphene and Graphene Layers. *Phys. Rev. Lett.* **2006**, *97*, No. 187401.
(48) Gao, Z.; Zhu, J.; Rajabpour, S.; Joshi, K.; Kowalik, M.; Croom, B.; Schwab, Y.; Zhang, L.; Bumgardner, C.; Brown, K. R.; Burden, D.; Klett, J. W.; van Duin, A. C. T.; Zhigilei, L. V.; Li, X. Graphene Reinforced Carbon Fibers. *Sci. Adv.* **2020**, *6*, No. eaaz4191.

https://doi.org/10.1021/acsanm.3c01199
ACS Appl. Nano Mater. XXXX, XXX, XXX−XXX

(49) Rosenburg, F.; Ionescu, E.; Nicoloso, N.; Riedel, R. High-Temperature Raman Spectroscopy of Nano-Crystalline Carbon in Silicon Oxycarbide. *Materials* **2018**, *11*, No. 93.
(50) Childres, I.; Jauregui, L. A.; Park, W.; Caoa, H.; Chena, Y. P. Raman Spectroscopy of Graphene and Related Materials. *New Dev. Photon Mater. Res.* **2013**, 403−418.
(51) Duy, L. X.; Peng, Z.; Li, Y.; Zhang, J.; Ji, Y.; Tour, J. M. Laser-Induced Graphene Fibers. *Carbon* **2018**, *126*, 472−479.
(52) Casiraghi, C. Doping Dependence of the Raman Peaks Intensity of Graphene Close to the Dirac Point. *Phys. Rev. B* **2009**, *80*, No. 233407.
(53) Gómez-Jeria, J. S.; Campos-Vallette, M. M.; Carrasco-Flores, E. A.; V, S. G. Raman and X-Ray Fluorescence to Identify Colors of the German Hyperinflation Stamps of the 1923 Collection. *J. Chil. Chem. Soc.* **2019**, *64*, 4622−4626.
(54) Caggiani, M. C.; Cosentino, A.; Mangone, A. Pigments Checker Version 3.0, a Handy Set for Conservation Scientists: A Free Online Raman Spectra Database. *Microchem. J.* **2016**, *129*, 123−132.
(55) Nwamba, O. C.; Echeverria, E.; McIlroy, D. N.; Shreeve, J. M.; Aston, D. E. Electrochemical Stability and Capacitance of In-Situ Synthesized Prussian Blue on Thermally-Activated Graphite. *SN Appl. Sci.* **2019**, *1*, No. 731.
(56) Nappini, S.; Matruglio, A.; Naumenko, D.; Dal Zilio, S.; Lazzarino, M.; De Groot, F. M. F.; Kocabas, C.; Balci, O.; Magnano, E. Graphene Nanoreactors: Photoreduction of Prussian Blue in Aqueous Solution. *J. Phys. Chem. C* **2017**, *121*, 22225−22233.
(57) Barsan, M. M.; Butler, I. S.; Fitzpatrick, J.; Gilson, D. F. R. High-Pressure Studies of the Micro-Raman Spectra of Iron Cyanide Complexes: Prussian Blue (Fe4[Fe(CN)6]3), Potassium Ferricyanide (K3[Fe(CN)6]), and Sodium Nitroprusside (Na2[Fe(CN)5(NO)]·2H2O). *J. Raman Spectrosc.* **2011**, *42*, 1820−1824.
(58) Qin, M.; Ren, W.; Meng, J.; Wang, X.; Yao, X.; Ke, Y.; Li, Q.; Mai, L. Realizing Superior Prussian Blue Positive Electrode for Potassium Storage via Ultrathin Nanosheet Assembly. *ACS Sustainable Chem. Eng.* **2019**, *7*, 11564−11570.
(59) You, Y.; Wu, X.-L.; Yin, Y.-X.; Guo, Y.-G. High-Quality Prussian Blue Crystals as Superior Cathode Materials for Room-Temperature Sodium-Ion Batteries. *Energy Environ. Sci.* **2014**, *7*, 1643−1647.
(60) Casimero, C.; Hegarty, C.; McGlynn, R. J.; Davis, J. Ultrasonic Exfoliation of Carbon Fiber: Electroanalytical Perspectives. *J. Appl. Electrochem.* **2020**, *50*, 383−394.
(61) Zhang, H.; Li, P.; Chen, S.; Xie, F.; Riley, D. J. Anodic Transformation of a Core-Shell Prussian Blue Analogue to a Bifunctional Electrocatalyst for Water Splitting. *Adv. Funct. Mater.* **2021**, *31*, No. 2106835.
(62) Li, X.; Chu, J.; Cheng, Y.; Yang, F.; Xiong, S. Novel Prussian Blue@Carbon-Dots Hybrid Thin Film: The Impact of Carbon-Dots on Material Structure and Electrochromic Performance. *Electrochim. Acta* **2020**, *355*, No. 136659.
(63) Wang, N.; Ma, W.; Du, Y.; Ren, Z.; Han, B.; Zhang, L.; Sun, B.; Xu, P.; Han, X. Prussian Blue Microcrystals with Morphology Evolution as a High-Performance Photo-Fenton Catalyst for Degradation of Organic Pollutants. *ACS Appl. Mater. Interfaces* **2019**, *11*, 1174−1184.
(64) Yang, J.; Huang, Z.; Yang, B.; Lin, H.; Qin, L.; Nie, M.; Li, Q. Green Route to Prussian Blue Nanoparticles with High Degradation Efficiency of RhB under Visible Light. *J. Mater. Sci.* **2021**, *56*, 3268−3279.
(65) Papakonstantinou, P.; Kern, R.; Robinson, L.; Murphy, H.; Irvine, J.; McAdams, E.; McLaughlin, J.; McNally, T. Fundamental Electrochemical Properties of Carbon Nanotube Electrodes. *Fullerenes, Nanotubes Carbon Nanostruct.* **2005**, *13*, 91−108.
(66) Lu, S. Y.; Chen, Y.; Fang, X.; Feng, X. Hydrogen Peroxide Sensor Based on Electrodeposited Prussian Blue Film. *J. Appl. Electrochem.* **2017**, *47*, 1261−1271.
(67) Ghaderi, S.; Mehrgardi, M. A. Prussian Blue-Modified Nanoporous Gold Film Electrode for Amperometric Determination of Hydrogen Peroxide. *Bioelectrochemistry* **2014**, *98*, 64−69.
(68) Bard, A. J.; Faulkner, L. R. *Electrochemical Methods Fundamentals and Applications*, 2nd ed.; John Wiley & Sons: Austin, 2001.

https://doi.org/10.1021/acsanm.3c01199
ACS Appl. Nano Mater. XXXX, XXX, XXX−XXX